The Journal of Chemical Physics ARTICLE scitation.org/journal/jcp

Exact semi-classical light–matter interaction operator applied to two-photon processes with strong relativistic effects

Cite as: J. Chem. Phys. 153, 024114 (2020); doi: 10.1063/5.0007833
Submitted: 17 March 2020 • Accepted: 22 June 2020 •
Published Online: 9 July 2020

Mickaël G. Delcey,[1] Rafael Carvalho Couto,[1,a)] Lasse Kragh Sørensen,[2] Ignacio Fdez. Galván,[3] Meiyuan Guo,[1] Roland Lindh,[3,b)] and Marcus Lundberg[1,c)]

AFFILIATIONS

[1]Department of Chemistry—Ångström Laboratory, Uppsala University, S-75120 Uppsala, Sweden
[2]Department of Theoretical Chemistry and Biology, School of Chemistry, Biotechnology and Health, KTH Royal Institute of Technology, SE-10691 Stockholm, Sweden
[3]Department of Chemistry—BMC, Organic Chemistry, Uppsala University, SE-75123 Uppsala, Sweden

[a)]**Also at:** Department of Theoretical Chemistry and Biology, School of Chemistry, Biotechnology and Health, KTH Royal Institute of Technology, SE-10691 Stockholm, Sweden.
[b)]**Also at:** Uppsala Center for Computational Chemistry (UC_3), Uppsala University, P.O. Box 576, SE-751 23 Uppsala, Sweden.
Electronic mail: roland.lindh@kemi.uu.se
[c)]**Author to whom correspondence should be addressed:** marcus.lundberg@kemi.uu.se

ABSTRACT

X-ray processes involve interactions with high-energy photons. For these short wavelengths, the perturbing field cannot be treated as constant, and there is a need to go beyond the electric-dipole approximation. The exact semi-classical light–matter interaction operator offers several advantages compared to the multipole expansion such as improved stability and ease of implementation. Here, the exact operator is used to model x-ray scattering in metal K pre-edges. This is a relativistic two-photon process where absorption is dominated by electric-dipole forbidden transitions. With the restricted active space state-interaction approach, spectra can be calculated even for the multiconfigurational wavefunctions including second-order perturbation. However, as the operator itself depends on the transition energy, the cost for evaluating integrals for hundreds of thousands unique transitions becomes a bottleneck. Here, this is solved by calculating the integrals in a molecular-orbital basis that only runs over the active space, combined with a grouping scheme where the operator is the same for close-lying transitions. This speeds up the calculations of single-photon processes and is critical for the modeling of two-photon scattering processes. The new scheme is used to model Kα resonant inelastic x-ray scattering of iron–porphyrin complexes with relevance to studies of heme enzymes, for which the total computational time is reduced by several orders of magnitude with an effect on transition intensities of 0.1% or less.

I. INTRODUCTION

Simulations of spectroscopic data are a critical tool for validation of calculations against experimental data. In chemistry, all spectroscopies depend on the interaction between the system and an external electromagnetic field. The field in the semi-classical approximation is typically described as a plane wave. However, in practice, the electric-dipole approximation is commonly used, which means that the electric field is treated as constant over the length-scale of the interacting system. This approximation has some important limitations. One example is high-energy photons where the short wavelength means that the electric field changes rapidly over the space of the target. This is, in particular, the case for metal K-edge x-ray absorption spectroscopy (XAS). Excitations from the 1s core orbital of first-row transition metals require photon energies of thousands of eV, hard x-rays, with corresponding wavelengths of 1 Å–2 Å.

A clear higher-order effect is that the 1s → 3d transitions in metal K pre-edges show significant absorption intensities despite being electric-dipole forbidden in centrosymmetric environments.[1]

Electric-dipole forbidden transitions have typically been handled by including higher-order terms in the multipole expansion, e.g., electric quadrupoles. For transitions with non-zero terms of lower order, the individual transition moments become origin dependent, which requires that the expansion is made to the same order as that in the oscillator strengths.[2] Second-order expansions thus require calculations up to magnetic quadrupoles and electric octupoles. Origin independence was originally shown for the velocity gauge,[2] but should also be valid in the length gauge.[3] Still, what is typically referred to as the length gauge is actually a mixed gauge, with the electric and magnetic components in the length and velocity gauges, respectively, and the mixed gauge does not preserve origin independence in finite basis sets.[3,4] Furthermore, the multipole expansion itself does not necessarily have a smooth convergence behavior toward the exact result.[5] Incorrectly evaluated higher-order expansions lead to spurious additional intensities that break the Thomas–Reiche–Kuhn sum rule.[6] A solution to the problems with the multipole expansion is to instead use the plane-wave form of the wave vector directly, which gives the exact semi-classical light–matter interaction.[5,7–10] No closed formula for the isotropically tensor averaged oscillator strengths is known, but the exact value can be approximated by averaging over different directions using a Lebedev grid.[8]

One area where the exact operator is of great value is for simulating the above-mentioned metal K pre-edges.[5,9] These spectra provide information about both geometric and 3d-electronic structures.[1] Hard x-rays are only weakly absorbed by lighter elements, which reduces background absorption and beam-induced sample damage. One disadvantage is that the short lifetime of the 1s core hole leads to significant lifetime broadening (1 eV–2 eV). High-resolution spectra that are rich in electronic structure information can be obtained using resonant inelastic x-ray scattering (RIXS).[11–14] Here, the incident energy (Ω) is scanned over the 1s → 3d absorption resonances followed by emission of a scattered photon of lower energy (ω); see Fig. 1.[13,15–21] For systems with low metal concentration or those that are rapidly damaged in the x-ray beam, it is preferable to monitor the most intense emission channel, Kα (2p → 1s), which is approximately ten times more intense than the Kβ (3p → 1s) emission.[15] The energy transfer, which is the difference between incident and emitted photons (Ω − ω), then corresponds to the energy of a 2p → 3d transition (metal L-edge XAS); see Fig. 1. As the lifetime of the 2p hole in the final state is longer than that of a 1s hole, this leads to a high resolution in the energy transfer direction even when using hard x-rays. High-resolution Kα RIXS data have been collected for several enzymes, e.g., photosystem II, cytochrome c, and hemoglobin.[18,22,23]

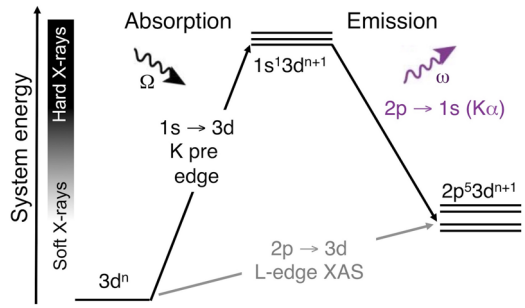

FIG. 1. Two-step total energy schematic of the Kα RIXS process. The vertical axis shows the total energy of the electron configuration.

In cytochrome c, RIXS was used to study the role of the axial ligands in electron transfer.[22] For hemoglobin, it was used to probe the extent of the electron transfer between iron and O_2.[23] In both cases, this information was extracted from comparisons with well-defined heme model complexes. Ideally, it should be possible to directly connect spectra to the electronic structure through a molecular-orbital (MO) model. This requires a method that handles strong correlation in open 2p and 3d shells, as well as spin–orbit coupling, which is especially strong for the 2p hole. At the same time, the spectra represent a relativistic two-photon process beyond the electric-dipole approximation. This is very challenging to describe using response theory, especially for highly correlated wavefunctions.

An electronic structure method that can describe these strongly correlated systems is the multiconfigurational restricted active-space (RAS) approach.[24,25] In this framework, multi-photon processes can be described using the the RAS state-interaction (SI) approach.[26,27] Here, spin–orbit coupling is introduced as a perturbation on top of a scalar relativistic wavefunction from a spin-free second-order Douglas–Kroll–Hess Hamiltonian.[28,29] The spectrum is then generated by combining individual transition moments between explicitly calculated initial, intermediate, and final spin–orbit states. This approach has previously been used to describe Kα RIXS of iron complexes using a second-order expansion.[30,31] However, for the reasons outlined above, the exact operator has many advantages in terms of stability, especially for systems where large basis sets are prohibitively expensive. A relativistic four-component implementation of the exact operator has been published,[5] but does not yet handle multi-photon processes. With restricted active space state-interaction (RASSI), the problem instead becomes the large number of transitions. For RIXS spectra, there can be hundreds or even thousands of spin–orbit states in each symmetry, which can give millions of individual state-to-state transitions. This is not a severe limitation in the electric-dipole approximation.[32] However, the form of the exact operator depends on the transition energy, and new integrals have to be calculated for every transition, which makes large RIXS calculations unfeasible.

To overcome this bottleneck, two new schemes have been implemented in OpenMolcas.[33] First, storage requirements and I/O computational overheads are reduced by storing integrals in the molecular-orbital (MO) basis running over active orbitals only, in contrast to the full atomic-orbital (AO) basis. Second, a modified plane-wave operator has been introduced that looks the same for groups of close-lying transitions. Combined, these two advances lead to computational savings of several orders of magnitude. The new implementation is used to model Kα RIXS of two iron–porphyrin complexes, ferrous (Fe^{II}) and ferric (Fe^{III}) Fe(P)(ImH)$_2$ (P = porphine, ImH = imidazole), of relevance for heme enzymes such as cytochrome c and hemoglobin.[22,23] X-ray spectroscopy gives unique

insights into the iron electronic structure in heme systems because the $\pi \rightarrow \pi^*$ transitions in the porphyrin ligand obscure UV/Vis probes of the metal.[34] L-edge XAS spectra of heme systems have been simulated with RAS,[35,36] but their RIXS spectra have previously only been modeled using the semi-empirical charge-transfer multiplet model.[22,23,37]

II. THEORY

This section gives a short background to the current implementation of the exact operator in OpenMolcas.[33] This is followed by a description of the main improvements in the new implementation that allows for calculations of a very large number of individual transitions.

A. Integral evaluations for the exact operator

Assuming that the electromagnetic field is weak, the external field can be treated as a perturbation of the molecular system. Starting from a monochromatic linearly polarized electromagnetic wave, the time-independent perturbation, when neglecting the spin-magnetic term, can be written as

$$\hat{U} = \frac{eA_0}{2m_e} \sum_i \exp(i\boldsymbol{k}\cdot\boldsymbol{r}_i)\left(\mathscr{E}\cdot\hat{\boldsymbol{p}}_i\right). \tag{1}$$

Here, $\boldsymbol{k}$ is the wave vector, $\mathscr{E}$ is the polarization direction, orthogonal to the direction of propagation $\boldsymbol{k}$, and lastly, $\boldsymbol{p}_i$ and $\boldsymbol{r}_i$ designate the momentum and position of the electrons, respectively. The two constants in the front, e and m_e, are the charge and mass of the electron, respectively, and A_0 is the amplitude of the field.

The transition rates between state 0 and n depend on the transition moment $T_{0n} = \langle 0 \mid \hat{T} \mid n\rangle$ with the transition operator $\hat{T}$ defined as $\hat{T} = \frac{2}{A_0}\hat{U}$. Thus, moving to atomic units, the key ingredient in evaluating the exact operator in a Gaussian basis is the evaluation of integrals of the following type:

$$I_\lambda^{\mu\nu} = \langle\chi_\mu|\exp(\pm i\boldsymbol{k}\cdot\boldsymbol{r})\hat{p}_\lambda|\chi_\nu\rangle, \tag{2}$$

where χ is a Gaussian basis function and $\hat{p}_\lambda$ is the momentum along a specific direction λ. The evaluation of the exact operator in the velocity representation in Eq. (2) can be performed in many different ways. The, perhaps, most intuitive way is as a Fourier transformation of a Gaussian where analytical recursive formulas are well known.[38] Alternatively, the $\exp(\pm i\boldsymbol{k}\cdot\boldsymbol{r})$ term can be evaluated as a sum of sine and cosine functions.[7,8] As the evaluation of the analytical expression involves a new Gaussian, these integrals can be evaluated using a standard Gauss–Hermite quadrature. OpenMolcas includes an elegant and efficient procedure to evaluate the integrals in this formalism.[9,10,33] As usual, these integrals are then multiplied by the transition density matrix Γ between the states a and b to form the expectation value of the transition operator,

$$\langle a|\hat{T}|b\rangle_\lambda = I_\lambda^{\mu\nu}\Gamma_{\mu\nu}^{ab}, \tag{3}$$

and the squared norm of the moment is used to calculate the oscillator strength. In the end, the isotropic oscillator strengths f_{ab} are obtained after the tensor averaging over a Lebedev grid.[8]

B. Exact operator for a large number of transitions

Irrespective of the way Eq. (2) is evaluated, every explicit state-to-state transition requires a new set of integrals due to the assumption of resonant excitations, which causes the wave vector $\boldsymbol{k}$ to be dependent on the excitation energy. This direct dependence of the excitation energy is the bottleneck for the exact operator and the only disadvantage compared to the regular multipole expansion. We will, therefore, seek approximations which remove this bottleneck.

First, we created a new implementation where the one-particle transition densities are computed once and stored on a disk in a compact MO format; for a wavefunction of active space SCF type, only explicit elements over the active orbitals are required. The one-particle transition densities are then retrieved from the disk and transformed to the AO basis as needed. This is opposed to the previous implementation that stored the one-particle transition densities over the full AO basis. This leads to a significant reduction in disk space storage, from n^2 to n_a^2 storage, which typically for the calculations presented here translates to a reduction in storage requirements of up to four orders of magnitude. Additionally, reducing the amount of information that is retrieved from permanent storage also leads to reductions in the I/O overhead and, thus, adds to the overall speed-up of the calculation.

Second, in order to further improve the efficiency, the number of sets of integrals needed in a calculation must be reduced. This can be accomplished by using the same integrals for energetically close transitions. For response methods, such as the complex polarization propagator (CPP) approach, where the excited state is not explicitly calculated, the number of different wave vectors will depend on the number of points needed to construct the spectrum.[39] Here, a related approach is applied where all transitions to final states within a certain energy range use the same wave vector $\boldsymbol{k}$. The numerical justification for this grouping of transitions is found by comparing how individual integrals over a set of basis functions in Eq. (2) vary with $\boldsymbol{k}$.

It can be shown that from grouping the transitions, the lowest-order change in an integral will be a first-order change in the transition moment,[10]

$$\Delta I_\lambda^\tau = \langle\chi_\mu|i\Delta k_\tau p_\lambda|\chi_\nu\rangle, \tag{4}$$

where ΔI_λ^τ is the change in the integral along the λ, τ-directions and $\Delta\boldsymbol{k} = \boldsymbol{k_a} - \boldsymbol{k_b}$ is the difference in $\boldsymbol{k}$ for two resonant transitions a and b. This can also be used to estimate the number of points needed to construct the spectrum for the CPP approach. Note that $\boldsymbol{k}$ and $\Delta\boldsymbol{k}$ share the same direction and only differ in their norm.

For the isotropically averaged oscillator strengths, the grouping of transitions will, therefore, only introduce a small change in the second-order terms in the oscillator strength $f_{ab}^{(2)}$ since the change in the transition moment is in first order. For dipole allowed transitions, where $f_{ab}^{(0)}$ dominates, some variation with $\boldsymbol{k}$ in the integrals for the higher-order terms of the oscillator strength $f_{ab}^{(n\geq 2)}$ will not matter because the higher-order terms in the multipole expansion are typically several orders of magnitude smaller than the electric-dipole oscillator strength $f_{ab}^{(0)}$. We can, thus, allow $\Delta\boldsymbol{k}$ to be very large without a significant loss of accuracy.

On the other hand, for very weak or dipole forbidden transitions, such as the 1s → 3d transitions, the approximation will introduce a change in the integrals for the leading terms in the multipole expansion $f_{ab}^{(n\geq 2)}$. However, from Eq. (4), it is seen that the relative error in the integral ($\frac{\Delta I}{I}$) then becomes approximately linear in $\frac{\|\Delta \boldsymbol{k}\|}{\|\boldsymbol{k}\|}$. The oscillator strengths are proportional to the square of the integrals, and thus, their error will also be to first order linear in $\frac{\|\Delta \boldsymbol{k}\|}{\|\boldsymbol{k}\|}$. Thus, if $\boldsymbol{k}$ is large, which is the case in the x-ray spectroscopy of transition metal complexes, the transition intensities will in all cases vary very little for energetically close-lying transitions ($\Delta \boldsymbol{k}$ small, relative to $\boldsymbol{k}$). Overall, the quality and speed-up from using the same integrals for multiple transitions will depend on the sizes of $\boldsymbol{k}$, $\Delta \boldsymbol{k}$, and the electric-dipole transition intensity. In the above arguments, we have assumed that the multipole expansion is well behaved in order to get an ordered estimate of the different terms in the multipole expansion. The conclusion reached is, however, independent of the behavior of the multipole expansion since multipole expansion is never performed.

In order to be as easy to use as possible, we chose the default value assuming the worst-case scenario, meaning dipole forbidden transitions. In this case, the relative error in the intensity is related to the size of $\Delta \boldsymbol{k}$ and $\boldsymbol{k}$. We, thus, chose a default grouping threshold of 0.1%, meaning that within each group, the ratio $\frac{\|\Delta \boldsymbol{k}\|}{\|\boldsymbol{k}\|}$ is lower than 10^{-3}. The algorithm then automatically forms the smallest number of groups possible while respecting this constraint. Unless otherwise stated, this value was chosen throughout this work. The integrals for the group correspond to the center of the group interval.

In addition to the modifications of the exact operator, we have implemented a stricter orthonormalization scheme for CASPT2-type wavefunctions in RASSI. The default RASSI implementation assumes that the Hamiltonian and overlap matrices between CASPT2 states are diagonal. However, using the core–valence separation means that we calculate ground and core-hole states separately, even when they are in the same irreducible representation and spin multiplicity.[40] This can lead to some non-orthogonality between ground and core-hole states, even if core orbital rotation is restricted during the restricted active space self-consistent field (RASSCF) optimization. For the electric-dipole operator, the parity selection rules ensure that there are no direct contributions from this overlap. The exact operator also shows no observable effects on the intensities. However, for the second-order expansion, the residual overlap can create spurious intensities with the second-order expansion. More specifically, the electric-quadrupole–electric-quadrupole contribution contains a term that is the product of the electric-quadrupole moments of initial and final states, and the overlap between the two states.

To correct this, an optional procedure is added to RASSI to ensure prior orthonormalization of states, even for CASPT2-type wavefunctions. First, the overlap matrix $\boldsymbol{S}$ is explicitly calculated. Second, using the overlap matrix, approximate off-diagonal elements are added to the Hamiltonian,

$$H_{ab} = 0.5(H_{aa} + H_{bb})S_{ab}, \tag{5}$$

with H_{ab} the Hamiltonian matrix element between states a and b and S_{ab} the corresponding overlap element. These terms prevent the final orthonormalization from leading to large shifts in the final energies. Finally, overlap and Hamiltonian matrices are diagonalized to get a new set of orthogonal states that can be used in the intensity calculations. This transformation completely removes the spurious second-order intensities, and the use of approximate off-diagonal elements introduces only a minor shift in energy. The shift depends on the energy difference between the states, but since the overlaps were small, even for the 7000 eV range in the K pre-edge calculations, the shifts were all below the meV range. Unless otherwise stated, the modified RASSI procedure has only been applied to the second-order calculations as they are the only ones showing spurious intensity contributions.

III. COMPUTATIONAL DETAILS

All RAS calculations are performed using OpenMolcas.[33] The design of the two heme models follows descriptions in Ref. 36. Both complexes belong to the C_{2h} point group. The strong ligand fields of the porphyrin and imidazole ligands lead to low-spin states. The ferrous d^6 complex has a singlet ($S = 0$) ground state, and the ferric d^5 complex has a doublet ($S = 0.5$) ground state.

The valence active space (RAS2) includes the five metal 3d-dominated orbitals; see Fig. 2. For simplicity, these orbitals will be labeled t_{2g} and e_g using the well-known O_h point group nomenclature. To these metal-centered orbitals, two filled ligand-dominated σ bonding orbitals are included as they correlate strongly with the empty anti-bonding e_g orbitals. The next step is to include three empty orbitals that can correlate with the filled t_{2g} orbitals. These are, unless specifically commented, metal 4d orbitals that describe the double-shell effect; see Fig. SI 1.[41] To describe the Kα RIXS process, the iron 1s orbital is placed in RAS3 and the iron 2p orbitals are included in RAS1.

Orbital optimizations were performed using state-average (SA) RASSCF, performed separately for each spin multiplicity and irreducible representation. To select relevant spin multiplicities, the selection rules for the spin–orbit operator ($\Delta S = 0, \pm 1$) were considered. For $Fe^{II}(P)(ImH)_2$, which has a singlet ground state, singlet and triplet intermediate and final states were included. For$Fe^{III}(P)(ImH)_2^+$, which has a doublet ground state, doublet and quartet states were included. Core-hole states are generated using a projection operator that selectively removes configurations with fully occupied core orbitals.[40] To avoid orbital rotation, i.e., the hole appears in a higher-lying orbital, the 1s and 2p core orbitals have been frozen in intermediate and final states.

Due to the wide energy range of the states, coupled with a high density-of-states, a large number of final states are required. The calculations take advantage of a new efficient configuration interaction algorithm to converge the state-average RASSCF calculations.[40] A detailed description of the number of states for each spin multiplicity and irreducible representation is given in the supplementary material (Table SI 1). Unless otherwise specified, the ANO-RCC-VDZP basis set[42,43] has been used in the resolution of identity approximation with an atomic-compact Cholesky decomposition-derived auxiliary basis.[44,45] Final energies were obtained with multi-state RASPT2 including all states from the SA-RASSCF calculations.[46] For the PT2 calculations, the default ionization-potential electron-affinity (IPEA) shift together with an imaginary shift of 0.3 hartree

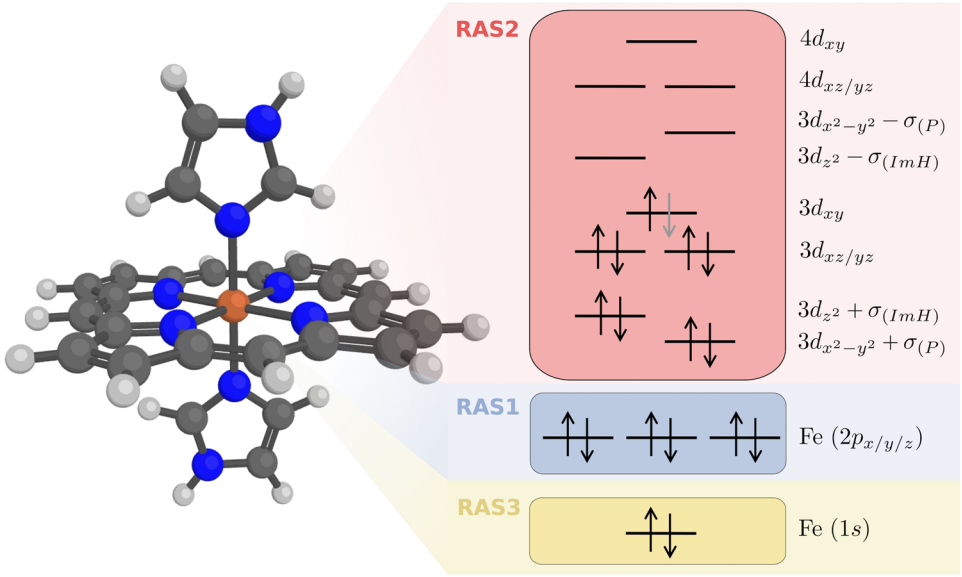

FIG. 2. Fe(P)(ImH)$_2$ (P = porphine, ImH = imidazole) model complex including active orbitals. The electron configuration with black arrows is for the ferric system. Contour drawings of the active orbitals are shown in Fig. SI 1.

has been used.[47,48] Simulated spectra are in some cases sensitive to the value of the IPEA shift,[49,50] but the L-edge XAS spectra of these heme complexes show only minor changes when varying the value of the IPEA shift.[36]

Scalar relativistic effects have been included by using a second-order Douglas–Kroll–Hess Hamiltonian,[28,29] and spin–orbit coupling is included by the RASSI approach.[26,27] RASSI has also been used to calculate transition moments, which have been combined to form the RIXS spectrum using the Kramers–Heisenberg formula,

$$F(\Omega,\omega) = \sum_f \left| \sum_i \frac{\langle f|\hat{T}_e|i\rangle\langle i|\hat{T}_a|g\rangle}{K(\Gamma_i)} \right|^2 \times K(\Gamma_f), \tag{6}$$

where the scattering intensity F is a function of incident energy (Ω) and emitted x-ray energy (ω), and $|g\rangle$, $|i\rangle$, and $|f\rangle$ are ground, intermediate, and final states, respectively. $K(\Gamma)$ depends on the resonance energy and the lifetime broadening Γ of each state. $\hat{T}_a$ and $\hat{T}_e$ are transition operators for the absorption and emission processes, respectively. For $\hat{T}_a$ and $\hat{T}_e$, we use the perturbation operator from Eq. (1) along with Fermi's golden rule. The current RIXS calculations use the oscillator strengths of absorption and emission processes, which means that interference effects are neglected. This corresponds to using this simplified formula,

$$F(\Omega,\omega) = \sum_f \sum_i |\langle f|\hat{T}_e|i\rangle|^2 |\langle i|\hat{T}_a|g\rangle|^2 \left| \frac{1}{K(\Gamma_i)} \right|^2 \times K(\Gamma_f). \tag{7}$$

Using this approximation allowed us to keep the code very general, instead of making it specific to RIXS processes, and is not expected to give any major error. However, in RASSI, the transition moments are, regardless, computed before the angular integration to form oscillator strengths, and thus, there is nothing formally preventing us to use them directly in the original Kramers–Heisenberg formula, restoring the full interference and the potential anisotropy. A Boltzmann averaging of the contributions from different initial states was made. For $Fe^{III}(P)(ImH)_2^+$, where six initial spin–orbit states contribute, the summation runs over up to 240 intermediate and 1440 final spin–orbit states. This gives more than 0.35×10^6 unique transitions and 4×10^6 unique pathways.

The electric-dipole operator is evaluated in both length and velocity representations. The second-order results are calculated in a mixed gauge, where the electric multipole terms are in the length representation, while the magnetic multipole terms are in the velocity representation.[3] This does not preserve origin independence, but for these calculations, there exists a natural choice of gauge origin at the iron atom, which is the center of the symmetry. Exact operator and group approximation are calculated in the velocity representation.[9]

Calculated spectra were broadened using a Lorentzian lifetime broadening of 1.25 eV full width at half maximum (FWHM) and a Gaussian experimental broadening of 0.2 eV in the incident energy direction.[51,52] This applies to both K pre-edge and RIXS spectra. L-edge XAS and energy transfer axes are broadened with 0.4 eV and 0.8 eV Lorentzians for the Kα_1 (L$_3$) and the Kα_2 (L$_2$) regions, respectively. The experimental broadening is set to 0.4 eV. Experimental RIXS spectra are taken from Ref. 22. Energies of the calculated spectra have been aligned with the first pre-edge peak, and intensities have been scaled to unity for the maximum of the pre-edge region. Energy shifts for all simulations are given in Table SI 2.

IV. RESULTS AND DISCUSSION

All x-ray processes in Fig. 1 will be modeled using both the multipole expansion and the exact operator. The first case is the metal L-edge XAS, which consists of electric-dipole allowed 2p → 3d transitions. The second case is the metal K pre-edge, with electric-dipole forbidden 1s → 3d transitions. Finally, the K pre-edge transitions are combined with electric-dipole allowed 2p → 1s emission to give the Kα RIXS spectra.

A. Iron L-edge XAS spectra

The simulated iron L-edge XAS spectra of the two heme complexes are shown in Fig. 3. The results for the electric-dipole approximation have been published previously.[36] The spectra have two separate edges, L_3 and L_2, split by the strong 2p spin–orbit coupling in the final state. The lower-energy L_3 edge of the ferrous heme spectrum is dominated by a main peak associated with transitions to the empty e_g orbitals. Still, this spectral feature includes contributions from a large number of final states; see Fig. 3. Comparing the spectra from the different transition moment operators shows that the spectral shapes are well preserved in all cases; see Fig. 3. Only the electric dipole in the length representation gives a visually different spectrum, which is not surprising considering our reference is the exact operator evaluated in the velocity representation. The deviations are still smaller than the difference between the experiment and simulations.[36]

The corresponding comparison for ferric heme gives similar results. This spectrum consists of a first sharp t_{2g} resonance, followed by a broader e_g resonance; see Fig. 3. The e_g resonance consists of a very large number of transitions to final spin–orbit states that are not even separated when plotted as individual sticks. With thousands of transitions, calculations with the exact operator are very costly, and electric-dipole calculations are instead compared to the group approximation. Again, the length representation gives a visually different spectrum, while the velocity representation overlaps almost perfectly with the grouped version of the exact operator.

The differences between approximations and the exact operator are shown in Fig. 4. To enable a visual comparison, the small deviations for the velocity representation and the group approximation are scaled up. The length representation consistently overestimates the intensity for both complexes. The deviations, relative to the intensity at the same point, also increase with increasing energy.

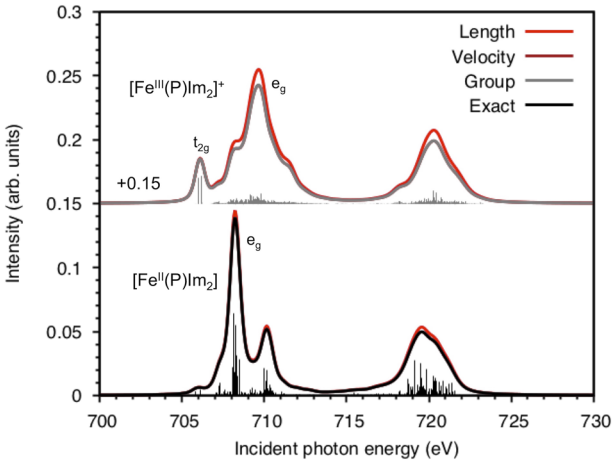

FIG. 3. L-edge XAS spectra of $Fe^{II}(P)(ImH)_2$ and $Fe^{III}(P)(ImH)_2^+$ models from RAS modeling using the exact operator, the group approximation, and the electric-dipole approximation in length and velocity representations. Sticks represent individual transitions, and due to the large number of contributions, there is a considerable overlap also in this representation.

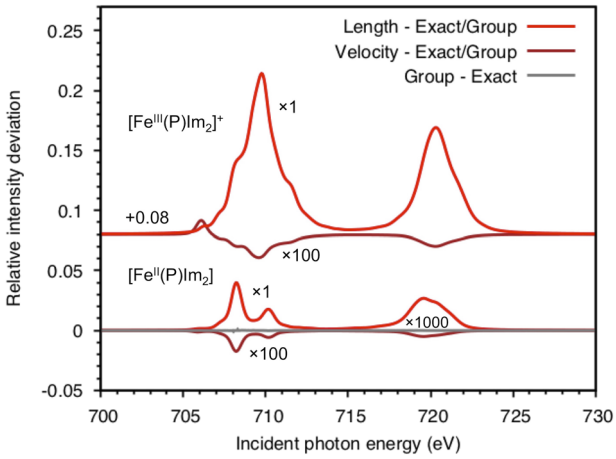

FIG. 4. Deviations between different operators for calculations of L-edge XAS spectra of heme models. For $Fe^{II}(P)(ImH)_2$, comparisons are made against the exact operator. For $Fe^{III}(P)(ImH)_2^+$, comparisons are made against the group approximation. Note the difference in scaling factors between the comparisons.

For the ferrous complex, the largest deviation, compared to the maximum intensity of the L_2 edge, reaches 4%. The errors are larger for the ferric complex, up to 16%. More detailed comparisons of individual transitions are shown in Table I. The deviations for the velocity representation are typically more than two orders of magnitude smaller, which again can be explained by the reference being also calculated in the velocity representation. It underestimates the intensity, with one exception, the t_{2g} resonance in the ferric complex. Finally, the group approximation shows virtually no deviations ($<10^{-5}$). This approximation is, thus, very accurate in the 700-eV transition region and clearly better even than the well-behaving velocity representation. As outlined in Sec. II, this is expected for electric-dipole allowed transitions.

B. K pre-edge XAS spectra

For the current centrosymmetric heme complexes, the K pre-edge XAS spectra consist of electric-dipole forbidden 1s → 3d transitions. These spectra have been calculated using the exact operator, the group approximation, and a second-order multipole expansion. Starting with the ferrous complex, the spectrum has a dominant pre-edge peak at 7112.2 eV; see Fig. 5. This pre-edge resonance comes from 1s → e_g transitions, and their splitting is small enough so that they appear as a single peak. The group approximation does not lead to any visible changes compared to the exact operator. The second-order expansion gives the same spectral shape but a slight increase in the intensity.

The pre-edge spectrum for the ferric complex has a significant additional structure. First, there is an additional transition to the partially open t_{2g} shell at 7111.2 eV. Second, the e_g peak with a maximum at 7112.9 eV consists of multiple resonances that come from open-shell coupling between the t_{2g} hole and the e_g electron; see Fig. 5.[1,30] This leads to a broader resonance with a significant structure, although individual transitions are obscured by the large lifetime broadening. Again, the group approximation gives essentially

TABLE I. Relative errors in intensity for multipole and group approximations compared to the exact operator. Multipole corresponds to electric-dipole transitions for metal L edges and a second-order expansion for metal K pre-edges.

		Multipole (length)		Multipole (velocity)		Grouping scheme	
Edge	System	RMSD	Max error	RMSD	Max error	RMSD	Max error
L-edge	$Fe^{II}(P)(ImH)_2$	6.22×10^{-2}	1.28×10^{-1}	2.46×10^{-3}	2.02×10^{-2}	1.28×10^{-6}	5.87×10^{-6}
	$Fe^{III}(P)(ImH)_2^+$	1.87×10^{-1}	1.90×10^{0}	3.44×10^{-3}	7.15×10^{-2}	...	...
K-edge	$Fe^{II}(P)(ImH)_2$	7.27×10^{-2}	1.29×10^{-1}	...	...	4.71×10^{-4}	8.13×10^{-4}
	$Fe^{III}(P)(ImH)_2^+$	8.51×10^{-2}	1.24×10^{-1}	...	...	4.68×10^{-4}	8.02×10^{-4}

the same spectral shape, while the second-order expansion gives a slight increase in the intensity.

To analyze the effects of the approximations to the transition operator, the differences compared to the exact operator are shown in Fig. 6 and Table I. For both systems, the deviations for the grouping scheme are below 0.1%. As explained in Sec. II, the difference between the two edges arises because for electric-dipole forbidden transitions, the group approximation introduces a change in the integrals already at the leading term. This explains the larger deviations compared to what was reported for the L-edge XAS spectra.

Interestingly, in both ferric and ferrous, the net effect of the grouping is a minor overestimation of the intensity. As mentioned in Sec. II, the approximation evaluates the operator for the energy at the center of the group interval and will, therefore, underestimate the intensity of about half of the transitions. Taking the ferric complex as an example, the average energy of the first group is at 7113.8 eV. The intensities of all transitions below this value are overestimated, while the transitions above are underestimated; see Fig. SI 2. The relative error is linearly proportional to the distance from the center. As the most intense transitions appear below 7113.8 eV, see Fig. 5, this leads to an overestimation of the total spectral intensity.

For both complexes, the second-order multipole expansion overestimates the intensity compared to the exact operator with deviations of around 7%–8%. This is similar to what was observed for the L-edge XAS spectra in the length gauge. It is possible that also this deviation is due to gauge differences, as the mixed-gauge second-order expansion in this case is dominated by the quadrupole–quadrupole term, which is in the length gauge. These results are obtained after correcting for artificial contributions from the residual non-orthogonality of initial and final states. Without these corrections, the second-order expansion shows additional high-energy transitions that in some cases are significantly more intense than the properly described transitions; see Fig. SI 3. These contributions do not appear when using the exact operator; see Fig. SI 4. The grouping scheme, thus, gives two orders of magnitude lower deviations than the second-order expansion with the additional benefit of decreased sensitivity to non-orthogonality.

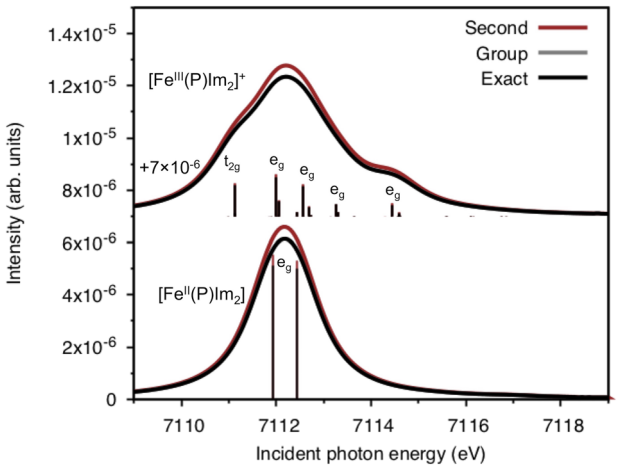

FIG. 5. Iron K pre-edge XAS spectra of $Fe^{II}(P)(ImH)_2$ and $Fe^{III}(P)(ImH)_2^+$ from RAS modeling using the exact operator, the group approximation, and the second-order multipole expansion. Spectra are calculated with the ANO-RCC-VDZP basis set using 40 and 80 final spin–orbit states for ferrous and ferric complexes, respectively. Sticks represent individual transitions.

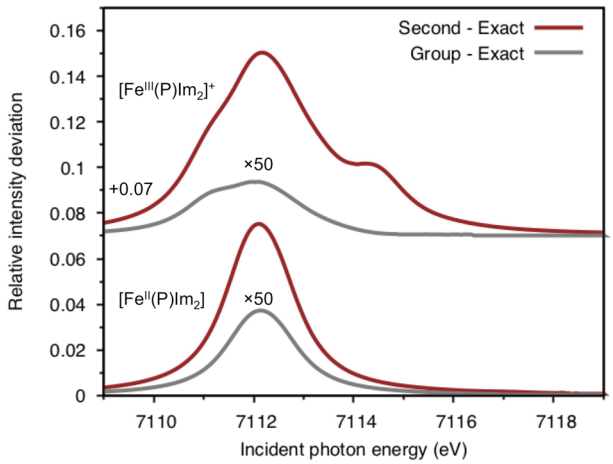

FIG. 6. Deviations between different operators for calculations of K pre-edge XAS spectra of heme models shown in Fig. 5. Note the different scales of the comparisons.

Increasing the size of the basis set from ANO-RCC-VDZP to ANO-RCC-VTZP leads to relatively minor changes in the simulated spectra; see Fig. SI 5. This is positive as it indicates that the pre-edge simulation is fairly well converged with a smaller basis set. Compared to the basis-set effect, the spectra are more sensitive to the number of final states. Increasing the number from 40 to 120 (20 and 60 per irreducible representation) has different effects on the two systems. For ferrous heme, it leads to the appearance of a high-energy π^* resonance that also appears in the experimental spectrum; see Fig. SI 6. For ferric heme, increasing the number of states results in a change in the active space which deteriorates the description of the e_g orbitals; see Fig. SI 1. The reference RIXS calculations will, therefore, be calculated using a different number of 1s core-hole states, 120 and 40 for ferrous and ferric heme, respectively.

C. RIXS

Experimental and modeled Kα RIXS spectra of ferrous and ferric heme are shown in Fig. 7. The two axes are the incident energy (Ω) and the energy transfer ($\Omega - \omega$). Each plane has two separate regions along the energy transfer axis. The region at lower energy is the Kα_1 emission, and these final states correspond to the L_3 edge of the L-edge XAS. The upper region is the Kα_2 emission, which corresponds to the L_2 edge. Note that the theoretical spectra have been calculated using the group approximation, as calculations with the exact operator could not be completed. The electric-dipole allowed transitions in the rising edge have been subtracted from the experimental spectra.[22] As the modeling does not include the rising edge, experiment and theory are directly comparable.

The experimental spectrum for ferrous heme has a pre-edge feature at 7112.2 eV; see Fig. 7(a). This is the previously discussed 1s → 3d(e_g) resonance. In addition to that main resonance, a high-energy absorption resonance is also visible in the experimental spectrum. In the energy transfer direction, the L_3 maximum is at 708.2 eV. The energy transfer is relatively broad, which indicates several emission resonances, some of which can be resolved. The simulated spectrum matches the experiment with a single dominant resonance that shows a clear structure along the energy-transfer axis; see Fig. 7(b). The energy splitting between the Kα_1 and Kα_2 regions is underestimated by 1 eV–2 eV, as seen in previous Kα RIXS simulations.[31] This can be explained by an underestimation of the 2p spin–orbit coupling in the present scheme.[53,54] A more detailed analysis of the energy transfer direction will be given below.

The ferric spectrum has two pre-edge features, associated with t_{2g} and e_g resonances as discussed above. The first feature, located at an incident energy of 7111.2 eV, is very sharp in the energy transfer direction, while the second one, with a maximum at 7112.9 eV, is much broader in both the incident energy and energy transfer directions; see Fig. 7(c). Both these features are also different in shape compared to the ferrous heme resonance. The calculations reproduce the experimental spectrum although the intensity of the e_g resonance is underestimated relative to the sharp t_{2g} peak. In addition, the shape of the e_g resonance is not completely reproduced, with some intensity lacking in the region closest to the t_{2g} peak. These deviations are similar to those seen in previous RAS simulations of iron hexacyanides.[31]

The full advantage of the high resolution in the RIXS experiment appears in the energy transfer direction. For ferrous heme,

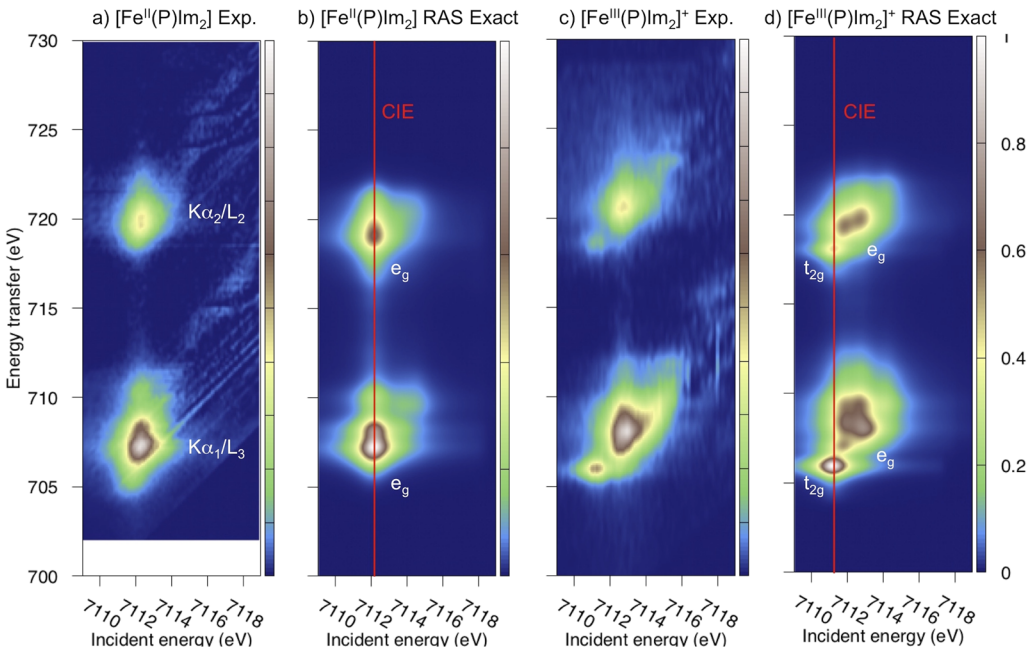

FIG. 7. Kα RIXS spectra of [(a and b)] $Fe^{II}(P)(ImH)_2$ and [(c and d)] $Fe^{III}(P)(ImH)_2^+$ from the experiment and RAS modeling using the grouping approximation. Experimental data from Ref. 22. The red vertical lines indicate the constant incident energy (CIE) cuts through the intensity maxima of the first resonances.

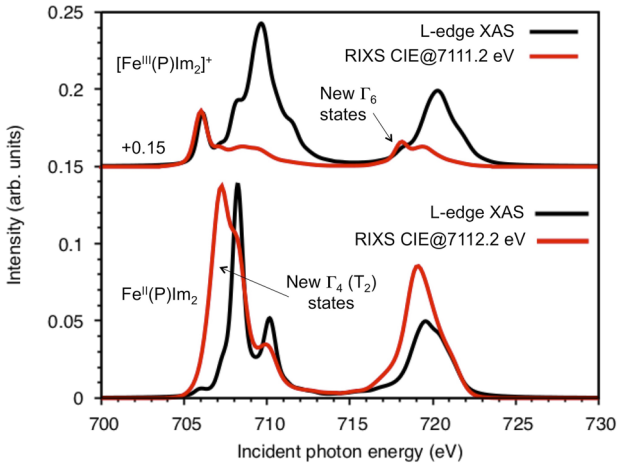

FIG. 8. L-edge RIXS cut vs CIE cut of RIXS spectra of ferrous and ferric heme. The positions of the CIE cuts are shown in Fig. 7.

an L-edge-like spectrum is obtained by taking a constant incident energy (CIE) cut through the maximum of the e_g resonance. The 2p → 1s emission from the ^1E_g intermediate states leads to $2p^5 3d^7$ final states, nominally the same as those in L-edge XAS. The L_3 edge of the simulated L-edge XAS spectrum has one main feature and a smaller high-energy feature. The CIE cut at 7112.2 eV incident energy gives a much wider e_g peaks, both in L_3 and L_2 edges; see Fig. 8. The same trend can also be observed in the experimental spectra.[22] As explained previously, the increased width can be explained by the difference in selection rules between the two experiments.[17] Using the nomenclature from O_h symmetry, the $2p^5 t_{2g}^6 e_g^1$ electron configuration has final states of both T_{1u} and T_{2u} symmetries. The L-edge XAS process only reaches T_{1u} states from the A_{1g} ground state, while the two-photon RIXS process reaches both T_{1u} and T_{2u} final states. Similar selection rules hold also for the D_{4h} point group.[22] The latter states are lower in energy because of more favorable 2p–3d electron interactions, which give rise to the apparent spectral broadening. The exact operator preserves these electric-dipole/quadrupole selection rules in this two-photon process.

For the ferric complex, the relatively weak t_{2g} peak in the L-edge XAS L_2 edge can be explained by the selection rules for the spin–orbit coupled states.[55] In the O_h point group, a direct excitation from the $J_{3d} = \frac{1}{2}$ ground state (Γ_7^+ in the Bethe double-group notation) to the L_2 $J_{2p} = \frac{1}{2}$ t_{2g} peak (Γ_6^-) is dipole forbidden. This rule is relaxed in the D_{4h} point group, but the corresponding peak is still much weaker in the L_2 edge. The CIE cut through that resonance correctly predicts a small increase in the intensity of the L_2 edge in the two-photon process. This illustrates that a non-relativistic implementation of the exact operator, combined with a perturbative approach to non-scalar relativistic effects, preserves the selection rules imposed by 3d and 2p spin–orbit couplings.

D. Timing comparisons

Comparisons of computation time between multipole expansion, the exact operator, and the group approximation are shown in Table II. All calculations, regardless of if they use only the multipole expansion or the exact operator, start with the computation of the transition density matrices in the biorthonormal basis in the RASSI program. This step is by far the most computational intensive when using the multipole expansion. Therefore, intensities obtained from the multipole approximation are always included even when computing the exact amplitudes. The computational time required to

TABLE II. Timing comparison (in min) of the different schemes. All calculations were performed on a single Intel Xeon Gold 6130 CPU. The values marked with a * refer to extrapolations based on the number of finished transitions after 12 days. For XAS calculations, initial and final states are listed. For RIXS calculations, initial, intermediate, and final states are listed.

Complex	Spectrum	Basis	Spin-free states	SOC states	SOC transitions	Standard	Exact operator	Grouped
$Fe^{II}(P)(ImH)_2$	L edge	ANO-RCC-VDZP	1/480	1/960	960	661	1 130	45
$Fe^{III}(P)(ImH)_2^+$	L edge	ANO-RCC-VDZP	3/480	6/1440	8640	683	18 709*	130
$Fe^{II}(P)(ImH)_2$	K pre-edge	ANO-RCC-VDZP	1/40	1/40	40	1	12	1
$Fe^{II}(P)(ImH)_2$	K pre-edge	ANO-RCC-VTZP	1/40	1/40	40	1	19	2
$Fe^{II}(P)(ImH)_2$	K pre-edge	ANO-RCC-VDZP	1/120	1/120	120	11	41	1
$Fe^{III}(P)(ImH)_2^+$	K pre-edge	ANO-RCC-VDZP	3/40	6/80	480	1	309	1
$Fe^{III}(P)(ImH)_2^+$	K pre-edge	ANO-RCC-VTZP	3/40	6/80	480	1	602	2
$Fe^{III}(P)(ImH)_2^+$	K pre-edge	ANO-RCC-VDZP	3/120	6/240	1 440	11	1 508	5
$Fe^{II}(P)(ImH)_2$	Kα RIXS	ANO-RCC-VDZP	1/40/480	1/40/960	38 440	612		245
$Fe^{II}(P)(ImH)_2$	Kα RIXS	ANO-RCC-VDZP	1/120/480	1/120/960	115 320	795	139 865*	718
$Fe^{III}(P)(ImH)_2^+$	Kα RIXS	ANO-RCC-VDZP	3/40/480	6/80/1440	115 680	756		481
$Fe^{III}(P)(ImH)_2^+$	Kα RIXS	ANO-RCC-VDZP	3/120/480	6/240/1440	347 040	813		1240

perform this step is shown in the table and called "Standard," while only the additional time for the exact operator is presented in the other columns.

For all calculations, the group approximation leads to significant reductions in computational time for the evaluation of the exact operator, often by two orders of magnitude or more. This is not critical for calculations up to around one thousand transitions, because then even the exact operator does not take much computational time, at least compared to the underlying electronic structure calculations. However, for some L-edge XAS calculations and all RIXS calculations, with tens or even hundreds of thousands of transitions, the calculations with the exact operator would take weeks or months on a single processor. The group approximation reduces this time to less than a day.

The effects of storing the transition densities in the basis of the active orbitals only instead of the full AO basis—transformation to the full AO basis is done on the fly as needed—are exemplified for the L-edge XAS calculation of $Fe^{II}(P)(ImH)_2$. It is among the smaller of the current calculations, but here, the AO basis requires a disk space of 234 GB. This is reduced by almost three orders of magnitude, down to 622 MB in the active orbital basis. Concurrently, the wall-clock time time is reduced by 10% due to the smaller I/O overhead.

For calculations using the group approximation, the group size is ~0.7 eV for the L-edge XAS spectra. As transitions span over ~20 eV, this gives around 30 groups. For the K pre-edge, the group size is 7.1 eV, which gives a single group for both complexes. In the emission calculations, the group size is 6.4 eV which gives five groups. Although the number of RIXS transitions remains the same, the total number of individual integrals is reduced to no more than six. The total cost of computing intensities with the exact operator using the grouping scheme is always on the same order of magnitude in timings as the standard RASSI, with multipole expansion being, at worst, 2.5 times as expensive. It is possible to modify timing and accuracy by changing this value, but the combination of small errors and excellent timing suggests that this value is appropriate. This means that in most cases, exact amplitudes can be computed without significantly hampering the efficiency.

V. CONCLUSIONS

The exact operator offers a number of advantages compared to the multipole expansion, including increased stability also for small basis sets. This has previously been implemented for single-photon processes. Here, it is extended to two-photon processes with significant relativistic effects through the state-interaction model, which makes it possible to also get two-photon processes in the context of the RASPT2 approach. However, with a very large number of transitions, the cost of evaluating the exact operator becomes very large as the operator itself and, thus, all integrals depend on the resonance energy. For the modeling of Kα RIXS, which can include hundreds of thousands of unique transitions in the state-to-state picture, this leads to a computational bottleneck. The new grouping scheme, where the form of the exact operator is the same for close-lying transitions, reduces the computational time by two orders of magnitude with minimal effects on the transition intensities. This computational approach is used to model heme complexes with good agreement between the experiment and theory. This opens up for *ab initio* modeling of Kα RIXS for both model complexes and enzymatic systems.

SUPPLEMENTARY MATERIAL

See the supplementary material for additional details about the RAS simulations including active orbitals and additional figures with K pre-edge XAS spectra.

ACKNOWLEDGMENTS

We acknowledge financial support from the Knut and Alice Wallenberg Foundation (Grant No. KAW-2013.0020). M.G.D. and M.L. acknowledge support from the Foundation Olle Engkvist Byggmastare (Grant No. 183-0403). R.C.C. and M.L. acknowledge support from the Carl Trygger Foundation (Grant No. CTS-17:297). L.K.S also acknowledges support from the Carl Trygger Foundation (Grant No. CTS-18:441). R.L. and I.F.G. acknowledge financial support from the Swedish Research Council (VR, Grant No. 2016-03398). The computations were performed on resources provided by SNIC through the National Supercomputer Centre at Linköping University (Tetralith) under Project Nos. snic-2018-3-575 and snic-2019-3-586.

DATA AVAILABILITY

The computer code is freely available from the OpenMolcas project in GitLab (https://gitlab.com/Molcas/OpenMolcas) under the Lesser General Public License (LGPL) (https://doi.org/10.1021/acs.jctc.9b00532).[33] Spectra and output files are available from the corresponding author upon reasonable request.

REFERENCES

[1] T. E. Westre, P. Kennepohl, J. G. DeWitt, B. Hedman, K. O. Hodgson, and E. I. Solomon, "A multiplet analysis of Fe K-edge 1s → 3d pre-edge features of iron complexes," J. Am. Chem. Soc. **119**, 6297–6314 (1997).

[2] S. Bernadotte, A. J. Atkins, and C. R. Jacob, "Origin-independent calculation of quadrupole intensities in X-ray spectroscopy," J. Chem. Phys. **137**, 204106 (2012).

[3] L. K. Sørensen, R. Lindh, and M. Lundberg, "Gauge origin independence in finite basis sets and perturbation theory," Chem. Phys. Lett. **683**, 536–542 (2017).

[4] L. K. Sørensen, M. Guo, R. Lindh, and M. Lundberg, "Applications to metal K pre-edges of transition metal dimers illustrate the approximate origin independence for the intensities in the length representation," Mol. Phys. **115**, 174–189 (2017).

[5] N. H. List, T. R. L. Melin, M. van Horn, and T. Saue, "Beyond the electric-dipole approximation in simulations of x-ray absorption spectroscopy: Lessons from relativistic theory," J. Chem. Phys. **152**, 184110 (2020).

[6] P. J. Lestrange, F. Egidi, and X. Li, "The consequences of improperly describing oscillator strengths beyond the electric dipole approximation," J. Chem. Phys. **143**, 234103 (2015).

[7] N. H. List, J. Kauczor, T. Saue, H. J. Aa. Jensen, and P. Norman, "Beyond the electric-dipole approximation: A formulation and implementation of molecular response theory for the description of absorption of electromagnetic field radiation," J. Chem. Phys. **142**, 244111 (2015).

[8] N. H. List, T. Saue, and P. Norman, "Rotationally averaged linear absorption spectra beyond the electric-dipole approximation," Mol. Phys. **115**, 63 (2017).

[9]L. K. Sørensen, E. Kieri, S. Srivastav, M. Lundberg, and R. Lindh, "Implementation of a semiclassical light-matter interaction using the Gauss-Hermite quadrature: A simple alternative to the multipole expansion," Phys. Rev. A **99**, 013419 (2019).
[10]M. Khamesian, I. Fdez. Galván, M. G. Delcey, L. K. Sørensen, and R. Lindh, "Spectroscopy of linear and circular polarized light with the exact semiclassical light–matter interaction," in *Annual Reports in Computational Chemistry* (Elsevier, 2019), Vol. 15, pp. 39–76.
[11]F. Gel'mukhanov and H. Ågren, "Resonant X-ray Raman scattering," Phys. Rep. **312**, 87–330 (1999).
[12]A. Kotani and S. Shin, "Resonant inelastic x-ray scattering spectra for electrons in solids," Rev. Mod. Phys. **73**, 203 (2001).
[13]L. J. P. Ament, M. van Veenendaal, T. P. Devereaux, J. P. Hill, and J. van den Brink, "Resonant inelastic x-ray scattering studies of elementary excitations," Rev. Mod. Phys. **83**, 705 (2011).
[14]M. Lundberg and P. Wernet, "Resonant inelastic x-ray scattering (RIXS) studies in chemistry: Present and future," in *Synchrotron Light Sources and Free-Electron Lasers: Accelerator Physics, Instrumentation and Science Applications*, edited by E. J. Jaeschke, S. Khan, J. R. Schneider, and J. B. Hastings (Springer International Publishing, Cham, 2020), pp. 2315–2366.
[15]P. Glatzel and U. Bergmann, "High resolution 1s core hole X-ray spectroscopy in 3d transition metal complexes—Electronic and structural information," Coord. Chem. Rev. **249**, 65–95 (2005).
[16]D. A. Meyer, X. Zhang, U. Bergmann, and K. J. Gaffney, "Characterization of charge transfer excitations in hexacyanomanganate(III) with Mn K-edge resonant inelastic x-ray scattering," J. Chem. Phys. **132**, 134502 (2010).
[17]M. Lundberg, T. Kroll, S. DeBeer, U. Bergmann, S. A. Wilson, P. Glatzel, D. Nordlund, B. Hedman, K. O. Hodgson, and E. I. Solomon, "Metal–ligand covalency of iron complexes from high-resolution resonant inelastic x-ray scattering," J. Am. Chem. Soc. **135**, 17121–17134 (2013).
[18]P. Glatzel, H. Schroeder, Y. Pushkar, T. Boron III, S. Mukherjee, G. Christou, V. L. Pecoraro, J. Messinger, V. K. Yachandra, U. Bergmann, and J. Yano, "Electronic structural changes of Mn in the oxygen-evolving complex of photosystem ii during the catalytic cycle," Inorg. Chem. **52**, 5642–5644 (2013).
[19]T. Kroll, M. Lundberg, and E. I. Solomon, "X-ray absorption and RIXS on coordination complexes," in *X-Ray Absorption and X-Ray Emission Spectroscopy* (John Wiley & Sons, Ltd., 2016), pp. 407–435.
[20]R. G. Hadt, D. Hayes, C. N. Brodsky, A. M. Ullman, D. M. Casa, M. H. Upton, D. G. Nocera, and L. X. Chen, "X-ray spectroscopic characterization of CO(iv) and metal–metal interactions in CO_4O_4: Electronic structure contributions to the formation of high-valent states relevant to the oxygen evolution reaction," J. Am. Chem. Soc. **138**, 11017–11030 (2016).
[21]E. Källman, M. Guo, M. G. Delcey, D. A. Meyer, K. J. Gaffney, R. Lindh, and M. Lundberg, "Simulations of valence excited states in coordination complexes reached through hard X-ray scattering," Phys. Chem. Chem. Phys. **22**, 8325–8335 (2020).
[22]T. Kroll, R. G. Hadt, S. A. Wilson, M. Lundberg, J. J. Yan, T.-C. Weng, D. Sokaras, R. Alonso-Mori, D. Casa, M. H. Upton, B. Hedman, K. O. Hodgson, and E. I. Solomon, "Resonant inelastic x-ray scattering on ferrous and ferric bis-imidazole porphyrin and cytochrome c: Nature and role of the axial methionine–Fe bond," J. Am. Chem. Soc. **136**, 18087–18099 (2014).
[23]J. J. Yan, T. Kroll, M. L. Baker, S. A. Wilson, R. Decréau, M. Lundberg, D. Sokaras, P. Glatzel, B. Hedman, K. O. Hodgson, and E. I. Solomon, "Resonant inelastic X-ray scattering determination of the electronic structure of oxyhemoglobin and its model complex," Proc. Natl. Acad. Sci. U. S. A. **116**, 2854–2859 (2019).
[24]J. Olsen, B. O. Roos, P. Jørgensen, and H. J. Aa. Jensen, "Determinant based configuration interaction algorithms for complete and restricted configuration interaction spaces," J. Chem. Phys. **89**, 2185–2192 (1988).
[25]P.-Å. Malmqvist, A. Rendell, and B. O. Roos, "The restricted active space self-consistent-field method, implemented with a split graph unitary group approach," J. Phys. Chem. **94**, 5477–5482 (1990).
[26]P.-Å. Malmqvist and B. O. Roos, "The CASSCF state interaction method," Chem. Phys. Lett. **155**, 189–194 (1989).
[27]P. Å. Malmqvist, B. O. Roos, and B. Schimmelpfennig, "The restricted active space (RAS) state interaction approach with spin–orbit coupling," Chem. Phys. Lett. **357**, 230–240 (2002).
[28]M. Douglas and N. M. Kroll, "Quantum electrodynamical corrections to the fine structure of helium," Ann. Phys. **82**, 89–155 (1974).
[29]B. A. Hess, "Relativistic electronic-structure calculations employing a two-component no-pair formalism with external-field projection operators," Phys. Rev. A **33**, 3742 (1986).
[30]M. Guo, L. K. Sørensen, M. G. Delcey, R. V. Pinjari, and M. Lundberg, "Simulations of iron K pre-edge X-ray absorption spectra using the restricted active space method," Phys. Chem. Chem. Phys. **18**, 3250–3259 (2016).
[31]M. Guo, E. Källman, L. K. Sørensen, M. G. Delcey, R. V. Pinjari, and M. Lundberg, "Molecular orbital simulations of metal 1s2p resonant inelastic x-ray scattering," J. Phys. Chem. A **120**, 5848–5855 (2016).
[32]I. Josefsson, K. Kunnus, S. Schreck, A. Föhlisch, F. de Groot, P. Wernet, and M. Odelius, "Ab initio calculations of x-ray spectra: Atomic multiplet and molecular orbital effects in a multiconfigurational scf approach to the l-edge spectra of transition metal complexes," J. Phys. Chem. Lett. **3**, 3565–3570 (2012).
[33]I. Fdez. Galván, M. Vacher, A. Alavi, C. Angeli, F. Aquilante, J. Autschbach, J. J. Bao, S. I. Bokarev, N. A. Bogdanov, R. K. Carlson, L. F. Chibotaru, J. Creutzberg, N. Dattani, M. G. Delcey, S. S. Dong, A. Dreuw, L. Freitag, L. M. Frutos, L. Gagliardi, F. Gendron, A. Giussani, L. González, G. Grell, M. Guo, C. E. Hoyer, M. Johansson, S. Keller, S. Knecht, G. Kovačević, E. Källman, G. Li Manni, M. Lundberg, Y. Ma, S. Mai, J. P. Malhado, P. Å. Malmqvist, P. Marquetand, S. A. Mewes, J. Norell, M. Olivucci, M. Oppel, Q. M. Phung, K. Pierloot, F. Plasser, M. Reiher, A. M. Sand, I. Schapiro, P. Sharma, C. J. Stein, L. K. Sørensen, D. G. Truhlar, M. Ugandi, L. Ungur, A. Valentini, S. Vancoillie, V. Veryazov, O. Weser, T. A. Wesołowski, P.-O. Widmark, S. Wouters, A. Zech, J. P. Zobel, and R. Lindh, "OpenMolcas: From source code to insight," J. Chem. Theory Comput. **15**, 5925–5964 (2019).
[34]R. K. Hocking, E. C. Wasinger, Y.-L. Yan, F. M. F. deGroot, F. A. Walker, K. O. Hodgson, B. Hedman, and E. I. Solomon, "Fe l-edge x-ray absorption spectroscopy of low-spin heme relative to non-heme Fe complexes: Delocalization of Fe d-electrons into the porphyrin ligand," J. Am. Chem. Soc. **129**, 113–125 (2007).
[35]M. Preuße, S. I. Bokarev, S. G. Aziz, and O. Kühn, "Towards an ab initio theory for metal l-edge soft X-ray spectroscopy of molecular aggregates," Struct. Dyn. **3**, 062601 (2016).
[36]M. Guo, E. Källman, R. V. Pinjari, R. C. Couto, L. Kragh Sørensen, R. Lindh, K. Pierloot, and M. Lundberg, "Fingerprinting electronic structure of heme iron by *ab initio* modeling of metal L-edge X-ray absorption spectra," J. Chem. Theory Comput. **15**, 477–489 (2019).
[37]F. de Groot, "Multiplet effects in X-ray spectroscopy," Coord. Chem. Rev. **249**, 31–63 (2005).
[38]J. Lehtola, M. Hakala, A. Sakko, and K. Hämäläinen, "ERKALE: A flexible program package for X-ray properties of atoms and molecules," J. Comput. Chem. **33**, 1572–1585 (2012).
[39]D. R. Rehn, A. Dreuw, and P. Norman, "Resonant inelastic x-ray scattering amplitudes and cross sections in the algebraic diagrammatic construction/intermediate state representation (ADC/ISR) approach," J. Chem. Theory Comput. **13**, 5552–5559 (2017).
[40]M. G. Delcey, L. K. Sørensen, M. Vacher, R. C. Couto, and M. Lundberg, "Efficient calculations of a large number of highly excited states for multiconfigurational wavefunctions," J. Comput. Chem. **40**, 1789–1799 (2019).
[41]K. Pierloot, "The CASPT2 method in inorganic electronic spectroscopy: From ionic transition metal to covalent actinide complexes," Mol. Phys. **101**, 2083–2094 (2003).
[42]B. O. Roos, R. Lindh, P.-Å. Malmqvist, V. Veryazov, and P.-O. Widmark, "Main group atoms and dimers studied with a new relativistic ANO basis set," J. Phys. Chem. A **108**, 2851–2858 (2004).
[43]B. O. Roos, R. Lindh, P.-Å. Malmqvist, V. Veryazov, and P.-O. Widmark, "New relativistic ANO basis sets for transition metal atoms," J. Phys. Chem. A **109**, 6575–6579 (2005).
[44]F. Aquilante, L. Gagliardi, T. B. Pedersen, and R. Lindh, "Atomic cholesky decompositions: A route to unbiased auxiliary basis sets for density fitting approximation with tunable accuracy and efficiency," J. Chem. Phys. **130**, 154107 (2009).

[45]J. Boström, M. G. Delcey, F. Aquilante, L. Serrano-Andrés, T. B. Pedersen, and R. Lindh, "Calibration of Cholesky auxiliary basis sets for multiconfigurational perturbation theory calculations of excitation energies," J. Chem. Theory Comput. **6**, 747–754 (2010).
[46]P. Å. Malmqvist, K. Pierloot, A. R. M. Shahi, C. J. Cramer, and L. Gagliardi, "The restricted active space followed by second-order perturbation theory method: Theory and application to the study of CuO_2 and Cu_2O_2 systems," J. Chem. Phys. **128**, 204109 (2008).
[47]N. Forsberg and P.-Å. Malmqvist, "Multiconfiguration perturbation theory with imaginary level shift," Chem. Phys. Lett. **274**, 196–204 (1997).
[48]G. Ghigo, B. O. Roos, and P.-Å. Malmqvist, "A modified definition of the zeroth-order Hamiltonian in multiconfigurational perturbation theory (CASPT2)," Chem. Phys. Lett. **396**, 142–149 (2004).
[49]R. V. Pinjari, M. G. Delcey, M. Guo, M. Odelius, and M. Lundberg, "Cost and sensitivity of restricted active-space calculations of metal l-edge X-ray absorption spectra," J. Comput. Chem. **37**, 477–486 (2016).
[50]E. Källman, M. G. Delcey, M. Guo, R. Lindh, and M. Lundberg, "Quantifying similarity for spectra with a large number of overlapping transitions: Examples from soft X-ray spectroscopy," Chem. Phys. **535**, 110786 (2020).
[51]M. O. Krause and J. H. Oliver "Natural widths of atomic K and L levels, Kα x-ray lines and several KLL Auger lines," J. Phys. Chem. Ref. Data **8**, 329–338 (1979).
[52]M. Ohno and G. A. van Riessen, "Hole-lifetime width: A comparison between theory and experiment," J Electron. Spectrosc. **128**, 1–31 (2003).
[53]N. Engel, S. I. Bokarev, E. Suljoti, R. Garcia-Diez, K. M. Lange, K. Atak, R. Golnak, A. Kothe, M. Dantz, O. Kühn, and E. F. Aziz, "Chemical bonding in aqueous ferrocyanide: Experimental and theoretical x-ray spectroscopic study," J. Phys. Chem. B **118**, 1555–1563 (2014).
[54]R. V. Pinjari, M. G. Delcey, M. Guo, M. Odelius, and M. Lundberg, "Restricted active space calculations of L-edge X-ray absorption spectra: From molecular orbitals to multiplet states," J. Chem. Phys. **141**, 124116 (2014).
[55]R. K. Hocking, E. C. Wasinger, F. M. F. de Groot, K. O. Hodgson, B. Hedman, and E. I. Solomon, "Fe L-edge XAS studies of $K_4[Fe(CN)_6]$ and $K_3[Fe(CN)_6]$: A direct probe of back-bonding," J. Am. Chem. Soc. **128**, 10442–10451 (2006).